Magnetic Resonance Imaging 62 (2019) 46–56

Contents lists available at ScienceDirect

Magnetic Resonance Imaging

journal homepage: www.elsevier.com/locate/mri

Original contribution

Blind deconvolution estimation of an arterial input function for small animal DCE-MRI

Radovan Jiřík[a,*], Torfinn Taxt[b], Ondřej Macíček[a], Michal Bartoš[c], Jiří Kratochvíla[a], Karel Souček[d,e,f], Eva Dražanová[a], Lucie Krátká[a], Aleš Hampl[g], Zenon Starčuk Jr.[a]

[a] Institute of Scientific Instruments of the Czech Academy of Sciences, Kralovopolska 147, 61264 Brno, Czech Republic
[b] Department of Biomedicine, University of Bergen, Jonas Lies vei 91, 5009 Bergen, Norway
[c] Institute of Information Theory and Automation of the Czech Academy of Sciences, Pod Vodarenskou vezi 4, 18208 Praha, Czech Republic
[d] Department of Cytokinetics, Institute of Biophysics of the Czech Academy of Sciences, Kralovopolska 135, 61265 Brno, Czech Republic
[e] Center of Biomolecular and Cellular Engineering, International Clinical Research Center, St. Anne's University Hospital Brno, Pekarska 53, 65691 Brno, Czech Republic
[f] Department of Experimental Biology, Faculty of Science, Masaryk University, Kotlarska 2, 61137 Brno, Czech Republic
[g] Department of Histology and Embryology, Faculty of Medicine, Masaryk University, Kamenice 3, 62500 Brno, Czech Republic

ARTICLE INFO

Keywords:
DCE-MRI
Blind deconvolution
Arterial input function

ABSTRACT

Purpose: One of the main obstacles for reliable quantitative dynamic contrast-enhanced (DCE) MRI is the need for accurate knowledge of the arterial input function (AIF). This is a special challenge for preclinical small animal applications where it is very difficult to measure the AIF without partial volume and flow artifacts. Furthermore, using advanced pharmacokinetic models (allowing estimation of blood flow and permeability-surface area product in addition to the classical perfusion parameters) poses stricter requirements on the accuracy and precision of AIF estimation. This paper addresses small animal DCE-MRI with advanced pharmacokinetic models and presents a method for estimation of the AIF based on blind deconvolution.

Methods: A parametric AIF model designed for small animal physiology and use of advanced pharmacokinetic models is proposed. The parameters of the AIF are estimated using multichannel blind deconvolution.

Results: Evaluation on simulated data show that for realistic signal to noise ratios blind deconvolution AIF estimation leads to comparable results as the use of the true AIF.

Evaluation on real data based on DCE-MRI with two contrast agents of different molecular weights showed a consistence with the known effects of the molecular weight.

Conclusion: Multi-channel blind deconvolution using the proposed AIF model specific for small animal DCE-MRI provides reliable perfusion parameter estimates under realistic signal to noise conditions.

1. Introduction

Dynamic contrast-enhanced (DCE) MRI is an important method characterizing the status of tissue microvasculature. This is important for diagnosis and assessment of response to treatment mainly in oncology [1]. Small animal (mice, rats) DCE-MRI [2] is an important tool for development of new drugs, typically for anti-cancer therapy, such as anti-angiogenic drugs [3–5].

The aim of this paper is to improve the quality of small animal quantitative DCE-MRI. In DCE-MRI, contrast agent concentration time curves of tissue regions of interest (ROI, e.g. the whole tumor or each voxel) are derived from MR image sequences acquired before, during and after contrast agent administration. In quantitative DCE-MRI, each tissue curve is approximated by an arterial input function (AIF) convolved with an impulse residue function (IRF) multiplied by plasma flow. The AIF is the contrast agent concentration curve in the arterial input of the tissue ROI. Estimation of a reliable AIF for each ROI is a challenge. Presently, it is one of the major factors causing low reliability of DCE-MRI.

Arterial input functions. There are several approaches to estimate the AIF. The first approach is to derive it from the acquired image sequence as the contrast agent concentration curve in a large artery [6]. However, such a measurement is distorted by flow artifacts, partial volume effects, saturation, T_2^* effects and dispersion. The partial volume artifact is more pronounced in small animal recordings. This is because of substantially smaller animal body size and the consequent need for coarser spatial resolution relative to the vessel size in small animal versus clinical DCE-MRI in order to achieve acceptable signal to noise

* Corresponding author.
E-mail address: jirik@isibrno.cz (R. Jiřík).

https://doi.org/10.1016/j.mri.2019.05.024
Received 3 January 2019; Received in revised form 2 May 2019; Accepted 19 May 2019

ratio (SNR). Flow artifacts are also more severe for small animal DCE-MRI because of higher ratio of flow velocity to slice thickness in small animals.

The second approach is to use a population based AIF [7]. This ignores the differences in the vascular tree between different individuals and depends on the AIF acquisition method and the contrast agent used for creation of these populations based “standards”.

The third approach is based on analysis of arterial blood samples taken during the bolus application [8]. It is a fairly invasive method and suffers from AIF shape dispersion (blood samples are taken far from the arterial input of the tissue ROI).

The fourth approach is based on a reference tissue (e.g. muscle) [9]. The AIF is estimated from the tissue curve in this reference tissue and the presumably known perfusion parameters. This approach has been shown for the Tofts model. For advanced pharmacokinetic models, the complete set of perfusion parameters in the reference tissue would have to be known, which is not realistic.

This paper is focused on a very different approach to estimate the AIF – blind deconvolution [10,11]. When imposing prior knowledge (e.g. positivity of the signals, a parametric AIF model and a parametric model for the IRF) and a suitable initial estimation scheme, it is possible to estimate simultaneously the parameters of the AIF and the perfusion parameters from the measured tissue ROI contrast agent concentration curves. This provides examination specific AIF estimates.

Impulse residue functions. In DCE-MRI, the usual pharmacokinetic models for the IRF are the Tofts and extended Tofts models [12,13]. The estimated perfusion parameters included in these models are the rate parameters K^{trans}, k_{ep} and v_e (and also v_p for the extended Tofts model), see Table 1 for description of perfusion parameters. To estimate a more complete perfusion parameter set, including blood plasma flow, F_p, and vessel permeability surface area product, PS, advanced pharmacokinetic models [12,13] must be applied. The most relevant are the two compartment exchange model (2CXM) [14], the tissue homogeneity model (TH) [15], the adiabatic approximation to the tissue homogeneity model (ATH) [16], the distributed parameter (DP) model [17], the distributed capillary adiabatic tissue homogeneity model (DCATH) [18], and the Gamma Capillary Transit Time (GCTT) model [11]. However, the parameter estimation of these advanced pharmacokinetic models requires a high SNR in order not to be ill-conditioned. Furthermore, application of these models assumes a high temporal resolution of the acquisition to capture the vascular distribution phase of the bolus. These are the main reasons why most quantitative DCE-MRI studies are based on the Tofts or extended Tofts models.

This paper is focused on blind-deconvolution AIF estimation in small animal DCE-MRI using advanced pharmacokinetic models. As a realistic AIF model is an important prior information, we concentrate on parametric AIF formulations. To the authors' knowledge, only two papers [19,20] have been published on this topic. They are based on an AIF model proposed originally for clinical DCE-MRI [10,11], described by 10 parameters, and do not contain any analysis of the accuracy and precision of the estimated AIFs.

The contribution of this paper is two-fold. First, we propose a 7-parameter AIF model taylored to small animal DCE-MRI to take advantage of the fact that a small animal AIF is usually of a simpler shape than a clinical AIF, see below. This reduction of AIF parameters (7 versus 10) helps to reduce the ill-conditioned character of blind deconvolution. Second, we propose an evaluation method on real data (where no ground-truth is available) based on use of two contrast agents with very different molecular weights. The known effects of the molecular weight on the shape of the AIF estimates are assessed. Furthermore, the consistency of the estimated perfusion parameters with the known effect of the contrast agent molecular weight is quantified. For example, the values of F_p and v_p should be molecular weight independent, while PS should decrease with increasing molecular weight [21–24]. This perfusion parameter evaluation approach has been used only in [24] for non-blind deconvolution (measured AIF) and it was applied to the mean signals of the tumor regions in a tumor canine model. We present a voxel-based analysis.

This work is a substantial extension of our initial study [25,26]. The proposed blind deconvolution AIF estimation method gave consistent results suggesting that it can be used as a reliable AIF estimation scheme.

Table 1
Description of symbols.

Quantity	Description	Unit
F_p	Plasma flow	mL/min/mL
PS	Permeability-surface area product	mL/min/mL
v_p	Plasma volume	mL/mL
v_e	Interstitial volume	mL/mL
K^{trans}	Volume transfer constant	1/min
k_{ep}	Interstitium-to-plasma rate constant	1/min
E	Extraction fraction	–
T_c	Capillary mean transit time	min
Δt	Delay between the common AIF and the ROI-specific local AIF	min
μ	Mean of the nontruncated normal distribution of T_c (DCATH model)	min
σ	standard deviation of the nontruncated normal distribution of T_c (DCATH model)	min
T_s	sampling interval	min

2. Material and methods

2.1. Perfusion modeling and parameter estimation

The tissue contrast agent concentration time curve in a ROI, $C(t)$, is given by the time-domain convolution of the AIF common for all ROIs, $C_p(t)$, and the delayed local IRF, $R(t-\Delta t)$, multiplied by the local plasma flow, F_p [13]:

$$C(t) = F_p \cdot C_p(t) * R(t-\Delta t) \quad (1)$$

The parameter Δt, is the delay between the common AIF and the ROI-specific local AIF, formulated as a part of the IRF as it is ROI specific.

Arterial input function. For the AIF, the standard model for small animal DCE-MRI is a bi-exponential function [27–29]. While this model is probably sufficient for the Tofts and extended Tofts pharmacokinetic models, it is not suitable for advanced pharmacokinetic models, such as the ATH model. The need for finer time domain sampling and more perfusion parameters inherent in these advanced IRF models require a more flexible AIF model. Especially the sharp peak of the bi-exponential AIF is unrealistic.

The AIF is a convolution of the bolus application function (contrast agent concentration versus time at the location of the cannula) and the remaining vascular distribution components. Assuming a typical case of a mouse examination with a constant speed of the contrast agent application (using a linear infusion pump) of 1 mL/min, the injection of a 0.1 mL dose of the contrast agent would take 6 s. This corresponds to the convolution of a rectangular blurring function of width 6 s with an ideal AIF which would be obtained for an instantaneous bolus application.

To model this blurring and to allow more degrees of freedom needed for a more detailed AIF, the AIF model proposed here is the sum of three gamma variate functions:

$$C_p(t) = t^{\beta} \sum_{n=1}^{3} \alpha_n e^{-\tau_n t}. \quad (2)$$

Here, t is time in minutes, while β, α_n and τ_n are the model parameters. To keep the number of AIF parameters low, the parameter β is

common for all three gamma variate functions. The number of gamma variate functions was set to three as a compromise between a too high flexibility of the AIF model and the need for a low number of AIF parameters, based on our preliminary experiments. The same number of gamma variate functions is used also in the clinical AIF model of [19,20] applied in the context of blind deconvolution in mice.

No delay between the gamma variate functions is modeled because the dynamics of the cardiovascular system in small animals is very fast and multiple passes of the contrast agent bolus are not visible in the AIF, contrary to the case of human AIFs. More specifically, for humans the whole blood volume is pumped through heart in approx. 1 min (cardiac output 5 L/min, blood volume 5 L [30]), while for mice in about 0.15 min (cardiac output 15 mL/min, blood volume 2.25 mL [30]). As in human AIF, the distance between the 1st and 2nd pass peaks is approx. 12 s [31], we can expect the corresponding distance in mice to be $12/1 \cdot 0.15 = 1.8$ s. Assuming the above described rectangular blurring function of width 6 s, the 2nd pass peak is very likely to be filtered out. In support of this assumption, no second pass peak is observable in measured mouse AIFs [27–29], nor in blind deconvolution AIF estimates of mice in [19] (Supporting information 3).

A more specific argument about the presence of the 2nd pass peak in mouse AIFs follows from a study in [32]. First, the authors state that the fastest application of the contrast agent bolus tolerated well by mice was 2 mL/min. With this maximal infusion-pump rate, lower volumes of the contrast-agent bolus (0.025 mL and 0.050 mL) were applied in murine DCE-MRI, corresponding to bolus administration durations of 0.75 s and 1.50 s. This led to a visible 2nd pass peak in the AIFs measured in the left ventricle. On the other hand, application of a full bolus (0.100 mL, bolus administration duration of 3 s), has blurred the 2nd pass peak out. This implies that the proposed AIF model (2) is suitable for a contrast-agent bolus of 0.100 mL or more, assuming the infusion-pump rate 2 mL/min, i.e. bolus administration duration of 3 s or more. This is the case of the most published studies on murine DCE-MRI.

Our AIF model could be treated as a simplified version of Schabel's AIF model [11,19], where we leave out the sigmoid curve and the delays between the gamma variate functions. An example of a measured AIF and its approximation by the proposed model is shown in Supplemental Fig. 1.

Tissue residue function. The constrained DCATH model of the IRF [18] is used here because of its continuous formulation of T_c, which leads to the advantage of a smooth transition between the vascular and parenchymal distribution phases of the IRF. Thus, the criterion function of the blind deconvolution task is continuous in T_c. This is in contrast to the more commonly used model ATH [33]. As in [34], a fixed dispersion of the capillary transit time T_c is used to decrease the number of free parameters and to avoid the ill-posed character of deconvolution when using the DCATH model [35]. With this simplification, the IRF model can be viewed as an approximation of the ATH model.

Using the assumption of a truncated normal distribution for T_c, the DCATH model of $F_p \cdot R(t)$ is parametrized by five parameters, $\Psi = \{F_p, E, k_{ep}, \mu, \sigma\}$ (see Table 1).

$$\begin{aligned} R(t) &= R_v(t) + R_p(t), \\ R_v(t) &= 1 - \frac{\mathrm{erf}\left(\frac{t-\mu}{\sqrt{2}\sigma}\right) + \mathrm{erf}\left(\frac{\mu}{\sqrt{2}\sigma}\right)}{1 + \mathrm{erf}\left(\frac{\mu}{\sqrt{2}\sigma}\right)} \\ R_p(t) &= E \exp\left(\frac{1}{2}k_{ep}^2\sigma^2 + k_{ep}(\mu - t)\right) \cdot \frac{\mathrm{erf}\left(\frac{t-\mu}{\sqrt{2}\sigma} - \frac{k_{ep}\sigma}{\sqrt{2}}\right) + \mathrm{erf}\left(\frac{\mu}{\sqrt{2}\sigma} + \frac{k_{ep}\sigma}{\sqrt{2}}\right)}{1 + \mathrm{erf}\left(\frac{\mu}{\sqrt{2}\sigma}\right)} \end{aligned} \tag{3}$$

The error function erf is defined as

$$\mathrm{erf}(t) = \frac{2}{\sqrt{\pi}} \int_0^t \mathrm{d}x \exp(-x^2). \tag{4}$$

The dispersion of T_c, σ, was fixed to T_s. This value is high enough to preserve the continuous formulation of the impulse residue function inherent to the DCATH model and low enough to consider the model as an approximation of the ATH model. A high value of σ is more likely to lead to a non-unique IRF model, see [35].

The mean of the nontruncated normal distribution of T_c, μ, is a good approximation of T_c [18] if the ratio σ/μ is sufficiently small (no greater than 1/3) [18]. This allows replacement of μ by T_c in (3).

With F_p and E known, the permeability surface area product, PS [mL/min/mL], is expressed as $PS = -F_p \ln(1 - E)$.

Similarly, v_p [mL/mL] and v_e [mL/mL] are given by $v_p = F_p \cdot T_c$ and $v_e = (E \cdot F_p)/k_{ep}$.

Parameter estimation. The first step is the estimation of the parameters of the common AIF, $C_p(t)$. The mean contrast agent concentration time curves in several manually selected ROIs (channels) are calculated. Then, the curves are simultaneously approximated by the convolutional model (1). This task is formulated as a minimization problem where the criterion function is a sum of squared differences between the samples of the contrast agent concentration time curve and its convolutional model for all channels. Hence, the blind deconvolution algorithm results in estimates of the $C_p(t)$ parameters (common for all channels) and of the IRF parameters and F_p (perfusion parameters) of each channel. The estimates of IRF parameters and F_p are not used in the subsequent processing.

The blind deconvolution algorithm starts with an initial AIF estimate and initial estimates of F_p and IRF. The minimization problem is solved by using an iterative alternating optimization scheme [10]. Each iteration (10 iterations are used here) consists of two parts: 1. Update of the IRFs' parameters and F_p of each channel while the AIF parameters are fixed to the actual estimate. 2. Update of the AIF parameters while the IRFs' parameters and F_p of each channel are fixed to the actual estimates. Each update is done using the Active-Set optimization algorithm as implemented in the Matlab™ Optimization toolbox (MathWorks, USA), function *fmincon*.

To account for the ROI-specific time delay between the estimated AIF and the tissue curve (i.e. the bolus arrival time), the IRF of each channel is formulated to include a delay parameter, Δt (see (1)). However, the time-domain sampling of the tissue curves causes discontinuities of the blind deconvolution criterion function [33]. In order to avoid this problem, the IRF delay is implemented as a convolution with a narrow Gaussian function of unity area under the curve and with the mean value equal to the delay. The width of this Gaussian function must be small enough to avoid any significant blurring of the IRF. It must also be high enough to avoid a discontinuous formulation of the delay due to the temporal undersampling of the Gaussian function.

By its nature, blind deconvolution provides estimation of the AIF shape, not its scale. A scaling factor needs to be estimated by an additional procedure, see Section 2.8.

After the common AIF has been estimated and scaled, it can be used in a voxel-by-voxel non-blind deconvolution calculating the perfusion parameter maps. The IRF model is the same as in the blind deconvolution (3) and the implementation is according to [35].

2.2. Simulated data

Synthetic data were generated as a convolution of a reference AIF (Fig. 1) and $F_p \cdot R(t - \Delta t)$ (see (1)), with additive Gaussian white noise. The sampling interval and the number of samples were as for the in vivo recordings (see below): $T_s = 1.05$ s, $N = 800$.

The reference AIF, $C_{p\ ref}(t)$, was a parametric AIF according to (2) derived from an AIF measured in aorta descendens in one of the in vivo recordings (Magnevist recording of mouse M1, see below). This measured AIF was selected manually based on visual assessment of the arterial voxel contrast agent concentration signals by selecting the signal with the steepest rising and falling parts and minimum noise. The measured AIF was then approximated by the AIF model (2) in order to obtain parameters of $C_{p\ ref}(t)$, see Supplemental Fig. 1.

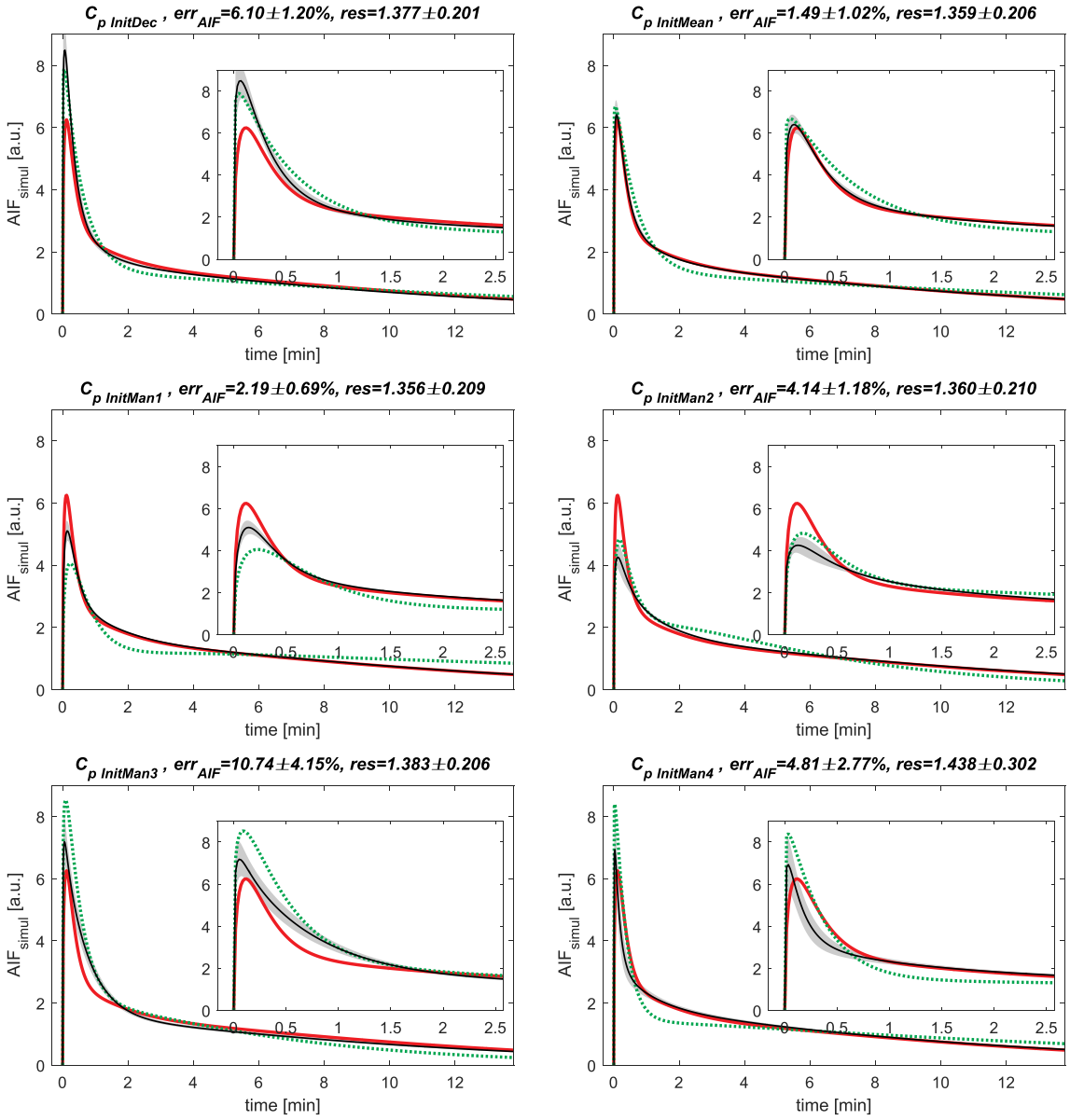

Fig. 1. AIF estimates for several initial AIFs, 6 channels, $SNR_{blind}=7$. Reference AIF (red line), AIF estimates – mean (solid black) ± standard deviation (gray area) and initial AIF estimates (dotted green). Plot titles: AIF estimation error – err_{AIF} (see (5)), sum of squares of fitting residuals – *res* (see (6)). AIFs normalized to unity area under the curve ×1000, a.u.: arbitrary units. (For interpretation of the references to colour in this figure legend, the reader is referred to the web version of this article.)

Two synthetic datasets were generated, one for evaluation of the blind deconvolution method alone and one for evaluation of its effect on the accuracy and precision of the subsequent voxel-by-voxel non-blind deconvolution. The first synthetic dataset (for testing of blind deconvolution) was generated for 5 SNR_{blind} levels, $W = 50$ noise realizations per SNR_{blind} level and 8 channels. This corresponded to $5 \cdot 50 \cdot 8 = 2000$ synthetic tissue curves.

For each of these tissue curves, different parameters of $F_p \cdot R(t - \Delta t)$ were chosen randomly (uniform distribution) within the following ranges: $F_p = [0.1 - 0.8]$ mL/min/mL, $E = [0.3 - 0.7]$, $T_c = \mu = [5 - 15]$ s and $v_e = [0.1 - 0.5]$ mL/mL ($k_{ep} = (E \cdot F_p)/v_e$). The Gaussian function modeling the IRF delay was used with a standard deviation $\sigma_{delay} = 0.06$ s and a random (uniform distribution) mean value in the interval $\Delta t = [0 - 2]$ s.

The noise was generated as a Gaussian random signal multiplied by a factor according to the intended level of SNR_{blind}. The SNR was defined as the mean of the noiseless signal ($F_p \cdot C_{p\ ref}(t) * R(t - \Delta t)$) divided by the standard deviation of the noise.

This synthetic dataset was used for the evaluation of the performance of the blind deconvolution algorithm with respect to the initial AIF estimate, SNR and the number of channels. For testing of the effect of the initial AIF estimate, the blind deconvolution algorithm was run using several different initial AIF estimates (i.e. initial parameters of the AIF model (2)).

The first initial AIF candidate, $C_{p\ InitDec}$, was the result of our initial study [25]. The second initial AIF candidate, $C_{p\ InitMean}$, was obtained from blind deconvolution of five recordings of this study (see Section 2.4, Magnevist recordings) by using the initial AIF estimate $C_{p\ InitDec}$ as follows: The mean of the five resulting AIF estimates was approximated by the AIF model (2), thus providing the parameters of $C_{p\ InitMean}$. Other initial AIF candidates, $C_{p\ InitManX}$, were generated by manual modification of the AIF model parameters so that the set of initial AIFs covered the cases with a narrow and broad peak and with a slow and a fast decay of the AIF tail.

2.3. Evaluation on simulated data

Quantitative evaluation of the AIF estimation was based on the relative AIF estimation error:

$$err_{AIF} = \frac{1}{WN}\sum_{w=1}^{W}\sum_{n=1}^{N}\frac{|C_{p\,w}[n] - C_{p\,ref}[n]|}{C_{p\,ref}[n]}\cdot 100\%, \quad (5)$$

where $C_{p\ w}[n]$ is the AIF estimate for the w-th noise realization. The time variable t has been replaced by the time index, n, to account for the time domain sampling and N is the number of samples. In addition to err_{AIF}, the sum of squares of the fitting residuals, res, was calculated over all channels as

$$res = \frac{1}{RN}\sum_{r=1}^{R}\sum_{n=1}^{N}(C_r[n] - \widehat{C}_r[n])^2. \quad (6)$$

Here, $C_r[n]$ is the synthetic contrast agent concentration sequence of the r-th ROI (channel), $\widehat{C}_r[n]$ is its approximation according to (1) given by blind deconvolution and R is the number of channels.

For the assessment of the accuracy of the voxel-by-voxel perfusion parameter estimates obtainable using the common blind deconvolution AIF estimate, non-blind deconvolution was applied to another set of synthetic contrast agent concentration sequences. These sequences were generated using the reference AIF, $C_{p\ ref}$, and three tumor types. The first was a prostate tumor ($F_p = 0.21$ mL/min/mL, $E = 0.65$, $T_c = 18.6$ s and $v_e = 0.35$ mL/mL [36]). The second was a glioblastoma ($F_p = 0.052$ mL/min/mL, $E = 0.161$, $T_c = 11.82$ s and $v_e = 0.076$ mL/mL [37]). The third was a colorectal tumor ($F_p = 0.256$ mL/min/mL, $E = 0.54$, $T_c = 15.5$ s and $v_e = 0.57$ mL/mL [19]).

For each tumor type and $SNR_{non-blind}$, $U = 200$ noise realizations were generated and added to the contrast agent concentration sequence. The perfusion parameter estimation error was quantified for each tissue and each $SNR_{non-blind}$ level as

$$err_{par} = \frac{1}{4UW}\sum_{u=1}^{U}\sum_{w=1}^{W}\left(\frac{|\widehat{F}_{p\,u,w} - F_{p\,ref}|}{F_{p\,ref}} + \frac{|\widehat{PS}_{u,w} - PS_{ref}|}{PS_{ref}} + \right.$$
$$\left. + \frac{|\widehat{v}_{p\,u,w} - v_{p\,ref}|}{v_{p\,ref}} + \frac{|\widehat{v}_{e\,u,w} - v_{e\,ref}|}{v_{e\,ref}}\right)\cdot 100\%. \quad (7)$$

Here, w is the index of the blind deconvolution AIF estimate (see (5)) and u is the index of noise realization added to the contrast agent concentration sequence of the given tumor type. The hat symbol denotes perfusion parameter estimates and the subscript "ref" stands for the reference value of the given perfusion parameter used in generation of the synthetic signal of the given tumor type.

A relative estimation error is evaluated also for each perfusion parameter separately.

2.4. Animal handling

The proposed AIF estimation method was evaluated on real data from five BALB/c mice (experiment approved by the National Animal Research Authority) with murine colon tumor cells CT26.WT (ATCC, CRL-2638) subcutaneously implanted into the left flank (10^6 cells in HC Matrigel). The mice were anesthetized with a mixture of isoflurane (2%) and O_2 (800 m L/min), and monitored continuously for respiratory rate and body temperature.

Each mouse was examined with two separate DCE-MRI recordings which were subsequently separately processed, the first one with a high molecular weight contrast agent (GadoSpin P, Miltenyi Biotec, Bergisch Gladbach, Germany, molecular weight 200 kDa), and the second one with a standard low molecular weight contrast agent (Magnevist, Bayer HealthCare Pharmaceuticals, Berlin, Germany, molecular weight 0.9 kDa). The delay between the bolus injections was 30 min. A high molecular weight contrast agent was injected first because its concentration can be assumed constant after 30 min, so that its effect on the tissue curves of the following low molecular weight contrast agent is minimized [24].

A linear infusion pump was used with injection speed of 1 mL/min. The dose of Magnevist was 0.3 mmol/kg weight. Magnevist was first diluted 1:5 with saline and 0.08 mL of this solution was injected, followed by 0.2 mL saline flush. For GadoSpin P, the dose of 0.1 mL of the supplied solution (25 mM gadolinium concentration) was applied, as recommended by the manufacturer, followed by the same saline flush as for Magnevist. When no mixing of the contrast agent and the saline flush is considered, for simplicity, the applied injection speed corresponds to the contrast agent injection duration of 4.8 s and 6 s for Magnevist and GadoSpin P, respectively.

2.5. MRI protocol

A 9.4 T BioSpin (Bruker Biospin MRI, Ettlingen, Germany) scanner was used. Anatomical images were recorded using the RARE sequence (T_2-weighted and T_1-weighted pre- and post-contrast). The parameter values for the T_2–weighted sequence were: TR/TE = 3500/36 ms, FOV 23×35 mm^2, image matrix 256×256, 20 axial slices with the thickness of 0.7 mm and no interslice gap. The parameter values for the T_1-weighted sequences were: TR/TE = 666/10 ms, with the same geometry as for the T_2-weighted sequence.

Before the first bolus administration, calibration scans were recorded and used for the conversion of the dynamic image sequences to the corresponding contrast agent concentration sequences. The acquisition was done using a 2D FLASH sequence with TR = 14, 30, 50, 100, 250, 500 ms, TE = 2.5 ms, flip angle 25°, image matrix 128×96 voxels, one axial slice located in the tumor center, slice thickness 1 mm, 15 images per sequence.

The DCE-MRI recordings (same acquisition parameters for both GadoSpin P and Magnevist recordings) were acquired using the 2D FLASH sequence with TR = 14 ms. The remaining parameters were the same as for the calibration scans. The sampling interval was 1.05 s and the acquisition time was 14 min (800 images).

2.6. Preprocessing

From multiple-TR calibration recordings, images of $k\rho$ (ρ is the spin density and k is a spatially invariant factor accounting for gain in the acquisition chain) and of the native T_{10} were obtained by approximation of the image data with the model of the FLASH acquisition (similarly to [38]), Eq. (6).

The multiple-TR method provides more reliable estimation than the standard method based on multiple flip angle recordings [38]. The multiple-TR method is less sensitive to B_1 field inhomogeneity and imperfections of the excitation profile of the RF pulses.

Subsequently, the same equation of the FLASH acquisition, including the estimated $k\rho$ values, was fitted to the DCE-MRI image data so that the relaxation rate $R_1[n]$ in each voxel at each time point n could be estimated. Then, the baseline, R_{10}, was estimated for each voxel as the mean R_1 in the time interval preceding the arrival of the contrast agent. The contrast agent concentration sequence of each voxel was calculated as $C[n] = (R_1[n] - R_{10})/r_1$ (assuming that the relaxivity r_1 is tissue independent).

The SNR of in vivo signals $C[n]$ was estimated as the mean of $C[n]$ divided by the standard deviation of the noise. The noise signal was estimated by approximation of the later part of $C[n]$ (i.e. a phase with slow changes, second half of $C[n]$ chosen here) by a second-order polynomial and subtraction of this polynomial from $C[n]$.

2.7. Initialization of blind deconvolution for real data

Due to local optima in the blind deconvolution optimization problem, the AIF estimate depends on its initial estimate. A possible solution would be to implement the blind deconvolution algorithm as a

global optimization scheme where the optimization would be performed several times, each time starting from a different initial AIF estimate. Then, the initial AIF estimate giving the best fit of the convolution model (1) to the tissue signals would be chosen. However, this approach resulted in a fairly high variability of the peaks of the AIF estimates when comparing different real data recordings with the same contrast agent.

Hence, another approach was chosen here. A common initial AIF estimate was set for all mouse recordings with both contrast agents and used as a common prior knowledge stabilizing the blind deconvolution algorithm. This initial AIF was found in two steps. First, the AIF was estimated several times by blind deconvolution with different initial AIF candidates. Then out of these initial AIF candidates the one giving the best fits over all recordings was selected as the single initial AIF.

Five initial AIF candidates were tested. The first initial AIF candidate, $C_{p\ InitDec}$, was the result of our initial study [25]. The second initial AIF candidate, $C_{p\ InitMean}$, was obtained from blind deconvolution Magnevist recordings of all five mice by using the initial AIF estimate $C_{p\ InitDec}$ as follows: The mean of the five resulting AIF estimates was approximated by the AIF model (2), thus providing the parameters of $C_{p\ InitMean}$. The other three candidates, $C_{p\ InitRagan}$, $C_{p\ InitCheckley}$ and $C_{p\ InitHeilmann}$, were derived from dual exponential AIFs from the literature [27–29] by imposing a smooth rising phase ($beta = 0.1$ for time in minutes in (2)) and setting the amplitude of the third AIF model term (α_3) to zero. The best fits of the convolution model (1) to the tissue signals were obtained in almost all in vivo recordings for the initial AIF estimate $C_{p\ InitMean}$. Thus, the results below are given for this initial AIF.

2.8. Blind deconvolution and AIF scaling for real data

Blind deconvolution was performed using 6 channels, each corresponding to a tumor voxel with a high SNR (manually selected in the nonnecrotic region).

AIF scaling was done for each recording. For each recording using Magnevist, a case specific area under the curve of the AIF, AUC_{Mag}, was derived according to the above mentioned reference tissue approach as follows. In the first step, the AIF was scaled approximatively based on the property of convolution stating that the area under the curve of a convolution result is the product of areas under the curves of the convolved functions. Thus, the area under the curve of $C_p(t)$ was calculated as the area under the curve of $C(t)$ in a reference tissue divided by the area under the curve of $F_pR(t)$. For the ATH model of $R(t)$, the area under the curve of $F_pR(t)$ is equal to $v_e + v_p$. Erector spinae muscle was used as the reference tissue, with the literature based value of $v_e + v_p$ of 0.13 mL/g according to v_e of mouse masseter muscle in [39] and assuming v_p to be 5% of v_e.

The above procedure neglected the fact that both $C(t)$ and $C_p(t)$ were sampled in a time limited window. Consequently, the available sequences did not decay completely to zero. This was taken into account by the following step.

The contrast agent concentration sequences of the reference region (erector spinae muscle) voxels were deconvolved with the approximatively scaled AIF. Then the median of $v_e + v_p$ estimated in the reference region was calculated. The ratio of this median and the literature value of $v_e + v_p$ was used for refinement of the AIF scale.

For GadoSpin P this procedure was not reliable because of low SNR. Instead, the AIF area under the curve for GadoSpin P, AUC_{GSP}, was calculated as $AUC_{GSP} = AUC_{Mag}(D_{GSP}r_{1GSP})/(D_{Mag}r_{1Mag})$, where D_{GSP} and D_{Mag} are contrast agent doses. The quantities r_{1GSP} and r_{1Mag} are the T_1 relaxivities for GadoSpin P and Magnevist, respectively. The relaxivities were measured in a separate in vitro experiment performed using the same NMR scanner. Using this procedure, we relied on a precise knowledge of the contrast agent doses.

2.9. Evaluation on real data

The variability of the blind deconvolution AIF estimates and the shape difference between the Magnevist and GadoSpin P groups were assessed visually. Perfusion parameters were validated based on their consistency with the expected effects of high and low molecular weight contrast agents. The intravascular parameters, v_p and F_p, should not be affected by the contrast agent molecular size. In contrast, PS should increase with decreasing molecular weight [19,21–23]. The volume of the extravascular extracellular space, v_e, should not be affected by the contrast agent molecular weight. However, a smaller fraction of this space might be accessible for high molecular weight contrast agent particles [40], leading to a possible underestimation of v_e.

The voxels for this evaluation were selected from manually drawn tumor regions (based on anatomical T_2-weighted images), excluding necrotic areas and fulfilling the condition of a sufficiently high SNR (SNR > 1) in both the Magnevist and GadoSpin P recordings. In necrotic regions, the usual pharmacokinetic models are not valid because the distribution of the contrast agent is affected by passive diffusion throughout neighboring voxel regions [2].

The voxels were assumed to be outside of necrotic areas when $k_{ep} > 0.2\ \mathrm{min}^{-1}$. This perfusion parameter was chosen because it is independent of AIF scaling and its maps were spatially consistent (more than the maps of another scaling independent parameter, E). The threshold of k_{ep} was selected from visual assessment of the perfusion parameter maps, T_2-weighted and post-contrast T_1-weighted anatomical images.

The estimated perfusion parameters were evaluated using boxplots, correlation coefficients and proportionality coefficients of the scatter plots, relating the perfusion parameters obtained for low and high molecular weight contrast agents.

3. Results

3.1. Simulated data

Arterial input functions. The peak of the estimated AIFs depended on the initial AIF estimate, while the AIF tail did not, as shown for a realistic $SNR_{blind} = 7$ (see Table 2 for SNRs of real data) and 6 channels (Fig. 1). The AIF estimation error (5) was related to the goodness of fit measure, res (Fig. 1). Lower res resulted mostly in a lower AIF estimation error.

The relative AIF estimation error (5) decreased when increasing the number of channels, as shown for realistic SNR_{blind} in Fig. 2 (a). The relative AIF estimation error also decreased when increasing SNR_{blind} (Fig. 2 (b)). In addition, for high SNR_{blind} (approx. for $SNR_{blind} > 5$), the AIF estimation error reflected a systematic error, i.e. accuracy limits due to the remaining level of ill-conditioning of the blind deconvolution process and due to numerical errors (Fig. 2 (b)). For low SNR_{blind} (approx. For $SNR_{blind} < 5$), the AIF estimation error reflected the precision limits due to the measurement noise.

Perfusion parameter estimates. Fig. 3 shows the mean relative error of the perfusion parameter estimates (7) in the subsequent nonblind deconvolution for the three tumor types (estimation errors of each single perfusion parameter are shown in Supplement fig. 2). As expected, the error decreased with increasing $SNR_{non-blind}$. In the ideal case, with the reference AIF, the error approached asymptotically zero (except for tissue 2). When using blind deconvolution AIF estimates, the perfusion parameter estimation error did not decrease below approx. 5%, even with high $SNR_{non-blind}$ for all three tumor types. This reflected the deviation of the blind deconvolution AIFs from the reference AIF. However, for the SNR observed in preclinical data ($SNR_{non-blind} < 10$), the achieved perfusion parameter estimation error was practically the same for the reference and blind deconvolution AIFs.

Table 2
Overview of mice recordings: numbers of analyzed voxels and SNRs for the Magnevist and GadoSpin P recordings, correlation and regression coefficients relating the perfusion parameters of the Magnevist recordings to the GadoSpin P recordings.

Mouse	No. of	SNR	SNR	Correlation coefficients				Regression coefficients			
no.	voxels	Magnevist	GadoSpin P	F_p	PS	v_p	v_e	F_p	PS	v_p	v_e
1	63	9.0	5.1	0.61	0.79	0.86	0.67	1.08	0.39	0.72	0.68
2	53	8.0	4.5	0.83	0.70	0.86	0.36	1.09	0.36	1.36	1.06
3	199	6.6	2.2	0.28	0.89	0.61	0.82	0.93	0.73	0.91	0.87
4	82	4.4	3.3	0.06	0.27	0.52	0.73	1.02	0.63	0.83	1.16
5	19	4.8	2.3	0.85	0.60	0.56	0.81	1.71	0.23	0.92	0.98
Mean	83	6.6	3.5	0.53	0.65	0.68	0.68	1.17	0.47	0.95	0.95
SD	69	2.0	1.3	0.35	0.24	0.17	0.19	0.31	0.21	0.24	0.18

3.2. Real data

The mean SNR values in the evaluated tumor voxels (nonecrotic, SNR > 1) were clearly higher for Magnevist compared to GadoSpin P (Table 2, columns 3, 4). This corresponded to higher extravasation rate of the low molecular weight contrast agent. The recordings from mice 1 and 2 had a clearly higher SNR than the other recordings. This was most probably due to higher volume fraction of vessels in the tumors of these mice, see below.

The contrast agent concentration sequences of the Magnevist and GadoSpin P recordings had a similar appearance (Supplement fig. 3). The decay of the GadoSpin P contrast agent concentration sequences was slower, compared to the Magnevist sequences. This reflected a slower renal clearance and a slower extravasation and intravasation of the high molecular weight contrast agent [21–23,40].

Arterial input functions. AIFs estimated for both Magnevist and GadoSpin P examinations had a low variance within each contrast agent group (Fig. 4). On the other hand, there was a clear difference between the mean AIFs of each contrast agent (Fig. 4) which was in line with the expected difference between high and low molecular weight contrast agents [21,40]. Compared to the mean Magnevist AIF, the mean GadoSpin P AIF had a broader peak. This reflected slower extravasation (i.e. a smaller extraction fraction, E) of GadoSpin P. The flatter later part of the mean GadoSpin P AIF reflected the smaller glomerular extraction rate of GadoSpin P.

Table 3 gives the parameters of the mean AIFs estimated from the Magnevist and GadoSpin P recordings. They were obtained by approximation of the mean contrast agent specific AIF (solid lines in Fig. 4) with the model (2). Each of the two mean AIFs was scaled using the median of AIF scaling factors (Section 2.4) calculated within the given contrast agent group.

Perfusion parameter estimates. The resulting DCE-MRI perfusion parameter maps (Fig. 5) were spatially consistent and in the expected range. They reflected the assumed histological composition. There was a clear distinction between the tumor rim and the more central part. High values of F_p and v_p in the outer lesion margin corresponded to a highly vascularized tumor rim.

In line with the theory, the estimates of F_p (Fig. 6) were not affected by the molecular weight of the contrast agent (with the exception of mouse 5).

The estimates of v_p (calculated as $v_p = F_p \cdot T_c$) were in good agreement with the expected molecular weight independence (Fig. 6). The parameter v_p was the intravascular perfusion parameter with the best agreement between the low and high molecular weight contrast agents.

The estimates of PS (Fig. 6) were clearly lower for the high molecular weight contrast agent, again in agreement with the known capillary membrane properties [21–23].

The estimates of v_e for the high and low molecular weight contrast agents were comparable, showing no clear trend of v_e with respect to the molecular weight of the contrast agent. In the recordings from mice 1 and 2, some values of v_e were higher than 1. This was probably due to AIF scaling problems, see discussion below. The boxplots of E, k^{ep} and T_c are shown and commented in Supplement Fig. 4.

The analysis of correlation and regression coefficients included F_p, v_p, PS and v_e. These perfusion parameters were the parameters where the physiological effect of the contrast agent molecular size was the easiest to interpret.

Table 2, columns 5–8, gives the correlation coefficient for each mouse and the selected perfusion parameters. Each correlation coefficient is for a single perfusion parameter estimated from the low and high molecular weight contrast agent recordings (see example scatter plots in Fig. 7).

There was a clear difference between the correlation coefficients estimated for the examined mice. For mice 1, 2 and 5 the achieved correlation coefficients were largely around 0.7. More variable values were achieved for mice 3 and 4. These mice had substantially lower F_p, PS and v_p values than mice 1, 2 and 5 (Fig. 6), which might be the explanation for the lower correlation coefficients. This was also partly

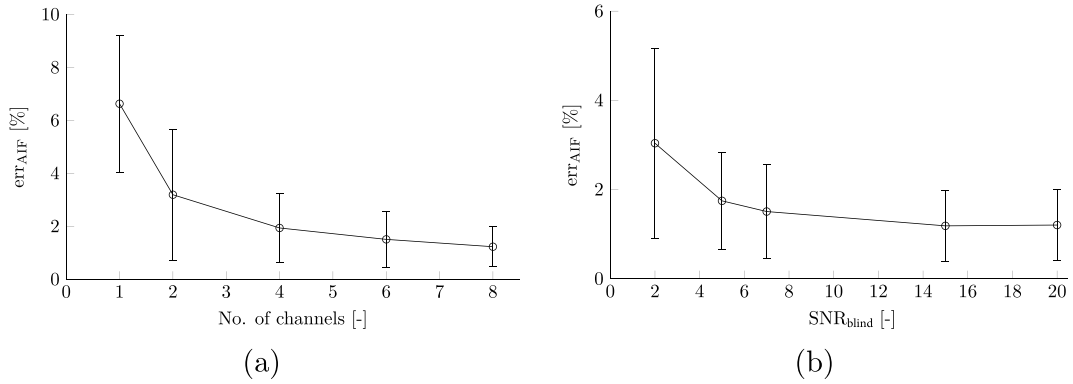

Fig. 2. AIF estimation errors. Initial AIF estimate: $C_{p\ InitMean}$. (a) AIF estimation error versus number of channels ($SNR_{blind}=7$). (b) AIF estimation error versus SNR_{blind} (6 channels). Confidence intervals defined as mean AIF estimation error (5) ± standard deviation of the results of the inner summation operation in (5).

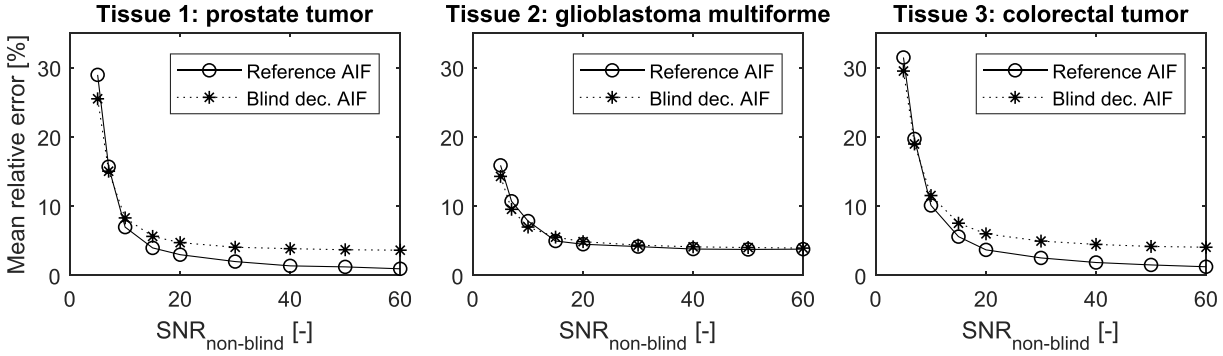

Fig. 3. Mean relative perfusion parameter estimation error (7) of non-blind deconvolution for the reference AIF and for blind deconvolution AIF estimates. Blind deconvolution AIFs were estimated from 6 channels with $SNR_{blind} = 7$, initial AIF estimate $C_{p\ InitMean}$. Three tissue types.

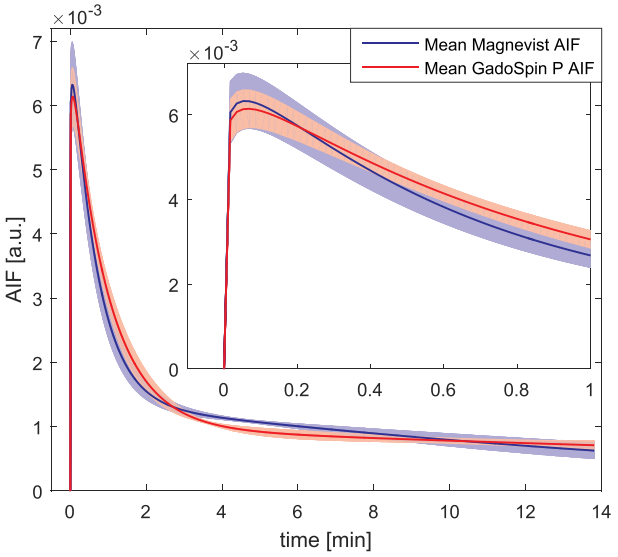

Fig. 4. AIFs estimated from Magnevist and GadoSpin P recordings. Shaded areas denote the mean ± standard deviation. AIFs normalized to unity area under the curve.

Table 3
Parameters of mean AIFs estimated from Magnevist and GadoSpin P recordings (see (2)).

Parameter [unit]	Magnevist	GadoSpin P
β [−]	0.0847	0.0755
α_1 [mM min$^{-\beta}$]	2.2540	0.6998
α_2 [mM min$^{-\beta}$]	0.8053	0.2597
α_3 [mM min$^{-\beta}$]	0.5381	0.1206
τ_1 [min^{-1}]	1.4330	0.9755
τ_2 [min^{-1}]	2.6349	2.3751
τ_3 [min^{-1}]	0.0700	0.0327

reflected by the SNR values (Table 2). The lowest correlation factors were observed for mouse 4, which was in line with the low SNR of its Magnevist recording.

The slopes of the regression curves estimated for each scatter plot (Table 2, columns 9–12) showed the consistency of the estimated perfusion parameters with the contrast agent molecular weight. The slopes of scatter plots for F_p, v_p and v_e were close to 1 (slope 1 corresponds to a perfusion parameter independent of the contrast agent molecular weight). The slope for PS was clearly lower than one, which corresponds to higher PS for low molecular weight contrast agents.

4. Discussion and conclusions

The presented blind deconvolution approach is based on an AIF model designed for small animal physiology and applied in combination with an advanced pharmacokinetic model.

So far, the only AIF model used for blind deconvolution AIF estimation in small animal DCE-MRI using an advanced pharmacokinetic model [19,20] was Schabel's model [11]. Here, we decrease the complexity of the AIF model by assuming a much faster blood recirculation in mice compared to humans. Hence no delay between the main and the recirculation peaks is modeled. This assumption is supported by the fact that no recirculation peaks are observable in Scabel's-model blind AIF estimates (supporting information 3 of [19]) and in the mouse AIFs measured in the left ventricle [27–29], as well as in our measurements in aorta descendens (Supplemental fig. 1).

Our proposed AIF model is not suitable for a low-volume contrast-agent bolus of 0.050 mL or less (assuming the fastest well tolerated infusion-pump rate 2 mL/min), prepared by application of a less diluted contrast agent [20] or a lower dose [32,41]. For such cases, Schabel's AIF model is more appropriate [11]. However, with lower bolus volumes, the uncertainty about the applied dose becomes high and requires additional correction, such as inductively coupled plasma-optical emission spectrometry proposed in [20].

Analysis of synthetic and real data showed a dependence of the peak of the blind deconvolution AIF estimate on the initial AIF estimate. The peak represents the high frequency band in the Fourier domain. Assuming model (1), this band is almost removed by the convolution of the AIF with the IRF because this operation acts like a low-pass filter. The retrieval of the AIF peak is the most demanding task of the algorithm. The above loss of information was overcome by applying good priors. It included relevant parametric models for the AIF and IRF, and a realistic initial AIF estimate.

Another possibility to cope with the dependence of the blind deconvolution on the initial AIF estimate is to use a global optimization approach where the curve fitting is repeated for several initial AIFs, and the best result in terms of fitting residuals is selected for each recording. This global optimization approach was also tested (data not shown). It led to worse results than the use of one fixed initial AIF estimate. This was because the best AIF solution might be found in a local rather than a global optimum, due to noise.

The fixed initial AIF estimate turned out to be an important part of prior information, preventing optimization from being trapped in an incorrect local or global optimum. From this point of view, the blind deconvolution AIF estimation can be understood as a method for the adjustment of a population based AIF so that it reflects the case specific vascular properties.

The results of this study show that a realistic case specific AIF can be estimated using the proposed blind deconvolution method. This conclusion is supported by the fact that a fairly small variation of the AIF

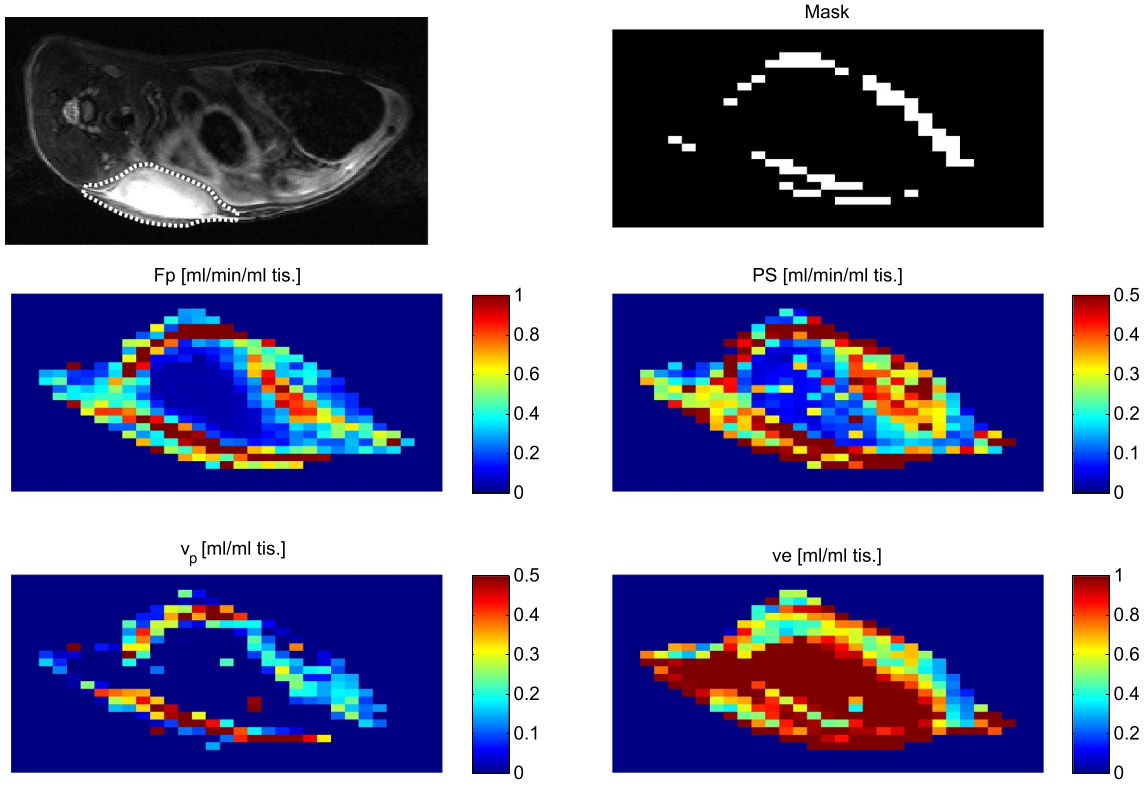

Fig. 5. Example images for mouse 2, Magnevist. T_2-weighted anatomical image (dotted line delineates the tumor, upper left region is a cross section of spine and spinal muscles). Estimated DCE-MRI perfusion parameter maps and the mask of high SNR voxels outside the necrotic area used for evaluation.

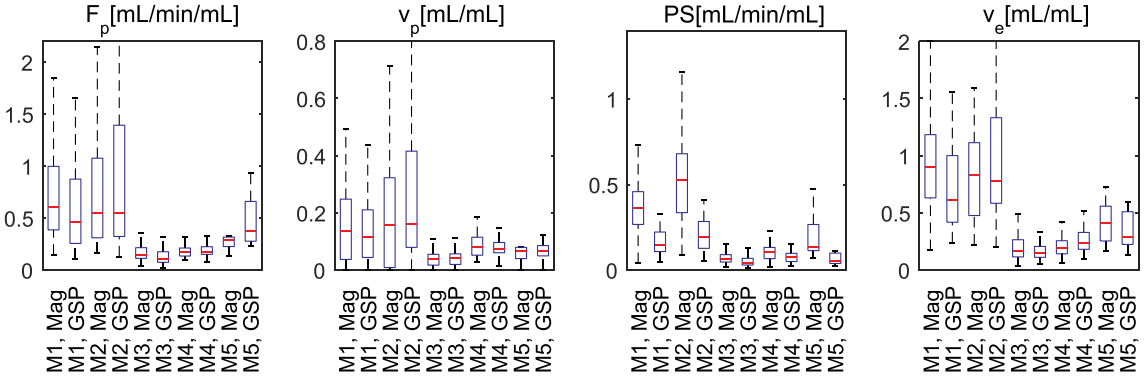

Fig. 6. Boxplots of estimated perfusion parameters. Mx – Mouse number, Mag – Magnevist, GSP – GadoSpin P.

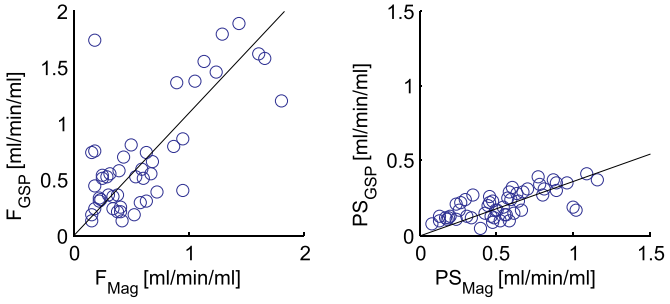

Fig. 7. Example of scatter plots and regression lines for mouse 2. Each circle corresponds to one high SNR voxel outside necrosis. Left: F_p, corr. coef. = 0.83, slope = 1.09. Right: *PS*, corr. coef. = 0.70, slope = 0.36.

estimates was observed within the contrast agent groups. In addition, a clear difference between the mean contrast agent specific AIFs was visible, which was according to the known differences in pharmacokinetics of the applied contrast agents.

Analysis of simulated data with $SNR_{non-blind}$ comparable to the SNR of in vivo data ($SNR_{non-blind} = 7$) showed that a similar accuracy of the perfusion parameter estimates can be achieved when using the correct (reference) AIF and when using a blind deconvolution AIF estimate.

The inaccuracy in blind deconvolution AIF estimation became visible in perfusion parameter estimates only for higher $SNR_{non-blind}$ of the synthetic voxel specific tissue curves ($SNR_{non-blind} > 10$). This shows that for real case SNRs, the accuracy of the perfusion parameter estimates is limited by the accuracy of the non-blind rather than the proposed blind deconvolution procedure. Our preliminary tests indicate

that more reliable perfusion parameter estimates can be obtained by the non-blind Lucy-Richardson algorithm in [43], probably due to its use of a non-parametric deconvolution prior to the parametric one. Also, the use of additional prior information taking the relationship of neighboring pixels into account, as in [44,45], will improve the performance of non-blind deconvolution.

The use of several contrast agents with different molecular weights in DCE-MRI based on advanced pharmacokinetic models has been proposed also in [19]. The prior information of the molecular weight independent perfusion parameters F_p, v_p and T_c was used in simultaneous fitting of multiple contrast agent curves. This led to more reliable perfusion parameter estimates. Here we propose to use this prior information solely for evaluation.

The differences in the physiological properties of the tumors (Fig. 6) and their SNR values (Table 2, columns 3, 4) had a clear effect on the achievable accuracy of the perfusion parameter estimates. The estimated perfusion parameters showed a higher plasma volume fraction of the tumors in mice 1, 2 and partly 5. There was also a higher SNR in these recordings than in the recordings of mice 3 and 4. The above two factors explain better consistency of the results with the two contrast agents observed for mice 1, 2 and partly 5, compared to mice 3 and 4.

The estimated correlation coefficients were still fairly low (Table 2, columns 5–8). This was probably the result of several factors. One factor degrading the correlation coefficient was motion of the mouse between (and during) the DCE-MRI acquisitions of the two contrast agents. This might be partly prevented by better fixation of the animal or by a respiration triggered acquisition. Respiration triggering would require a more sophisticated method coping with the impaired steady state of the FLASH acquisition due to nonconstant TR. A saturation-recovery prepared FLASH acquisition might be a good method of choice [24]. This would however lead to a decreased temporal and/or spatial resolution.

The procedure for AIF scaling is another source of inaccuracy of the perfusion parameter estimates. It might be too simplistic to assume the same $v_e + v_p$ for the erector spinae muscle of all mice, even if the same measurement conditions are kept. Also, the reference literature based value for $v_e + v_p$ might deviate from the true value. The literature values for skeletal muscles vary in a fairly wide range depending on the measurement method and the physiological state of the tissue. These scaling factor errors might be the reason for high v_e values, especially visible for mice 1 and 2 in Fig. 6 where $v_e > 1$ for some voxels. Another possibility would be scaling with respect to the “tail” level of a measured AIF. This approach was not reliable here due to a high variability in the arterial signal related mostly to its variable contamination by the partial volume effect and motion artifacts.

The reliability of the present blind deconvolution method might be further improved in several ways. A reparametrization of the applied pharmacokinetic model might help to improve the conditioning of the blind deconvolution process. Another possibility is to find a more realistic AIF model with parameters of a known physiological range connected with application of constraints on these parameters. To use more additional information, a combination of DCE-MRI with another MRI technique, such as DSC-MRI, might be considered [46].

The choice of the model might be another source of inaccuracy. The ATH model (implemented as a constrained DCATH model) was chosen as one of the available 4-parameter models. Other 4-parameter models include the 2CXM, TH and DP models. The 5-parameter models, such as the DCATH and GCTT models, were not considered due to the potentially worse conditioning of the approximation problem [35]. The choice of the ATH model was motivated by our previous comparisons of the 2CXM versus ATH in the context of blind deconvolution [43,47]. The ATH model could be also implemented as a constrained GCTT model. Whether the constrained GCTT model, the TH or DP model would lead to more reliable results is an open question to be addressed. These models are more realistic and might lead to better results, providing that the complexity of their corresponding criterial functional is comparable with the used ATH model.

In summary, we believe that this study may contribute to the acceptance of blind deconvolution for AIF estimation in small animal DCE-MRI. Our results showed that reliable perfusion parameter estimates can be obtained for a sufficiently high, but still realistic SNR.

Supplementary data to this article can be found online at https://doi.org/10.1016/j.mri.2019.05.024.

Acknowledgements

This study was supported by the Czech Science Foundation (GA16-13830S), Ministry of Education, Youth and Sports of the Czech Republic (CZ.1.05/2.1.00/01.0017, LO1212, LQ1605, CZ.02.1.01/0.0/0.0/16_013/0001775), The Czech Academy of Sciences (RVO:68081731), by the project ICRC-ERA-Human Bridge (No. 316345) funded by the 7th Framework Programme of the European Union and by the project HistoPARK – Centre for analysis and modeling of tissues and organs (Reg. no.: CZ.1.07/2.3.00/20.0185). We are also grateful to Eva Janoušová for consultations on evaluation methods.

References

[1] Jackson A, Buckley DL, Parker GJM. Dynamic contrast-enhanced magnetic resonance imaging in oncology. Berlin: Springer Science & Business Media; 2005.
[2] Barnes SL, Whisenant JG, Loveless ME, Yankeelov TE. Practical dynamic contrast enhanced MRI in small animal models of cancer: data acquisition, data analysis, and interpretation. Pharmaceutics 2012;4(3):442–78.
[3] Lee L, Sharma S, Morgan B, et al. Biomarkers for assessment of pharmacologic activity for a vascular endothelial growth factor (VEGF) receptor inhibitor, PTK787/ZK 222584 (PTK/ZK): translation of biological activity in a mouse melanoma metastasis model to phase I studies in patients with advanced colorectal cancer with liver metastases. Cancer Chemother Pharmacol 2006;57(6):761–71.
[4] Keunen O, Johansson M, Oudin A, et al. Anti-VEGF treatment reduces blood supply and increases tumor cell invasion in glioblastoma. Proc Natl Acad Sci U S A 2011;108(9):3749–54.
[5] Obad N, Espedal H, Jirik R, et al. Lack of functional normalisation of tumour vessels following anti-angiogenic therapy in glioblastoma. Journal of Cerebral Blood Flow & Metabolism 2018;38(10):1741–53.
[6] Pike MM, Stoops CN, Langford CP, et al. High-resolution longitudinal assessment of flow and permeability in mouse glioma vasculature: sequential small molecule and SPIO dynamic contrast agent MRI. Magn Reson Med 2009;61(3):615–25.
[7] Loveless ME, Halliday J, Liess C, et al. A quantitative comparison of the influence of individual versus population-derived vascular input functions on dynamic contrast enhanced-MRI in small animals. Magn Reson Med 2012;67(1):226–36.
[8] Verhoye M, van der Sanden BPJ, Rijken PFJW, et al. Assessment of the neovascular permeability in glioma xenografts by dynamic T1 MRI with Gadomer-17. Magn Reson Med 2002;47(2):305–13.
[9] Heisen M, Fan X, Buurman J, ter Haar Romeny BM. Effects of reference tissue AIF derived from low temporal resolution DCE-MRI data on pharmacokinetic parameter estimation. ISMRM-ESMRMB Joint Annual Meeting 2010. Sweden, Stockholm, Stockholm. 2010. p. 4802.
[10] Fluckiger JU, Schabel MC, DiBella EVR. Model-based blind estimation of kinetic parameters in dynamic contrast enhanced (DCE)-MRI. Magn Reson Med 2009;62(6):1477–86.
[11] Schabel MC, Fluckiger JU, DiBella EVR. A model-constrained Monte Carlo method for blind arterial input function estimation in dynamic contrast-enhanced MRI: I. simulations. Phys Med Biol 2010;55(16):4783–806.
[12] Sourbron SP, Buckley DL. Tracer kinetic modelling in MRI: estimating perfusion and capillary permeability. Phys Med Biol 2012;57(2):R1–33.
[13] Sourbron SP, Buckley DL. Classic models for dynamic contrast-enhanced MRI. NMR Biomed 2013;26(8):1004–27.
[14] Brix G, Kiessling F, Lucht R, Darai S, Wasser K, Delorme S, et al. Microcirculation and microvasculature in breast tumors: pharmacokinetic analysis of dynamic MR image series. Magn Reson Med 2004;52(2):420–9.
[15] Johnson JA, Wilson TA. A model for capillary exchange. Am J Physiol 1966;210(6):1299–303.
[16] St Lawrence KS, Lee TY. An adiabatic approximation to the tissue homogeneity model for water exchange in the brain: I. Theoretical derivation. J Cereb Blood Flow Metab 1998;18(12):1365–77.
[17] Larson KB, Markham J, Raichle ME. Tracer-kinetic models for measuring cerebral blood flow using externally detected radiotracers. J Cereb Blood Flow Metab 1987;7(4):443–63.
[18] Koh TS, Zeman V, Darko J, et al. The inclusion of capillary distribution in the adiabatic tissue homogeneity model of blood flow. Phys Med Biol 2001;46(5):1519–38.
[19] Jacobs I, Strijkers GJ, Keizer HM, Janssen HM, Nicolay K, Schabel MC. A novel approach to tracer-kinetic modeling for (macromolecular) dynamic contrast-enhanced MRI. Magn Reson Med 2016;75(3):1142–53.
[20] Hectors SJ, Jacobs I, Lok J, et al. Improved evaluation of Antivascular Cancer

therapy using constrained tracer-kinetic modeling for multiagent dynamic contrast-enhanced MRI. Cancer Res 2018;78(6):1561–70.
[21] Zhou Z, Lu Z-R. Gadolinium-based contrast agents for magnetic resonance cancer imaging. Wiley Interdiscip Rev Nanomed Nanobiotechnol 2013;5(1):1–18.
[22] Delrue LJ, Casneuf V, Van Damme N, et al. Assessment of neovascular permeability in a pancreatic tumor model using dynamic contrast-enhanced (DCE) MRI with contrast agents of different molecular weights. Magnetic Resonance Materials in Physics, Biology and Medicine 2011;24(4):225–32.
[23] Daldrup H, Shames DM, Wendland M, et al. Correlation of dynamic contrast-enhanced MR imaging with histologic tumor grade: comparison of macromolecular and small-molecular contrast media. AJR Am J Roentgenol 1998;171(4):941–9.
[24] Henderson E, Sykes J, Drost D, et al. Simultaneous MRI measurement of blood flow, blood volume, and capillary permeability in mammary tumors using two different contrast agents. J Magn Reson Imaging 2000;12(6):991–1003.
[25] Jiřík R, Souček K, Dražanová E, et al. Blind multichannel deconvolution for estimation of a parametric AIF in DCE-MRI of mice. ISMRM proceedings 2014. vol. 4. 2014. p. 2754.
[26] Jiřík R, Souček K, Mézl M, et al. Blind deconvolution in dynamic contrast-enhanced MRI and ultrasound. 36th Conf. Of the IEEE engineering in medicine and biology society 2014. 2014. p. 4276–9.
[27] Heilmann M, Walczak C, Vautier J, et al. Simultaneous dynamic T1 and T2* measurement for AIF assessment combined with DCE MRI in a mouse tumor model. Magma 2007;20(4):193–203.
[28] Ragan D, Lai S, Bankson J. Fast, reproducible measurement of the vascular input function in mice using constrained reconstruction and cardiac sampling. NMR Biomed 2011;24:373–84.
[29] Checkley D, Tessier J, Wedge S, et al. Dynamic contrast-enhanced MRI of vascular changes induced by the VEGF-signalling inhibitor ZD4190 in human tumour xenografts. Magn Reson Med 2003;21:475–82.
[30] Treuting PM, Dintzis SM, Montine KS. Comparative anatomy and histology: A mouse, rat and human atlas. London: Academic Press; 2017.
[31] Parker GJM, Roberts C, Macdonald A, et al. Experimentally-derived functional form for a population-averaged high-temporal-resolution arterial input function for dynamic contrast-enhanced MRI. Magn Reson Med 2006;56(5):993–1000.
[32] van Nierop BJ, Coolen BF, Dijk WJ, Hendriks AD, de Graaf L, Nicolay K, et al. Quantitative first-pass perfusion MRI of the mouse myocardium. Magn Reson Med 2013;69(6):1735–44.
[33] Koh TS, Cheong DLH, Hou Z. Issues of discontinuity in the impulse residue function for deconvolution analysis of dynamic contrast-enhanced MRI data. Magn Reson Med 2011;66(3):886–92.
[34] Kratochvíla J, JiÅ™ík R, Bartoš M, et al. Distributed capillary adiabatic tissue homogeneity model in parametric multi-channel blind AIF estimation using DCE-MRI. Magn Reson Med 2016;75(3):1355–65.
[35] Bartoš M, Jiřík R, Kratochvíla J, et al. The precision of DCE-MRI using the tissue homogeneity model with continuous formulation of the perfusion parameters. Magn Reson Imaging 2014;32(5):505–13.
[36] Kershaw LE, Buckley DL. Precision in measurements of perfusion and microvascular permeability with T1-weighted dynamic contrast-enhanced MRI. Magn Reson Med 2006;56(5):986–92.
[37] Schabel MC. A unified impulse response model for DCE-MRI. Magn Reson Med 2012;68(5):1632–46.
[38] Li K-L, Zhu XP, Waterton J, Jackson A. Improved 3D quantitative mapping of blood volume and endothelial permeability in brain tumors. J Magn Reson Imaging 2000;12(2):347–57.
[39] Reed RK, Viig H. Compliance of the interstitial space in rats. I. Studies on hindlimb skeletal muscle. Acta Physiol Scand 1981;113(3):297–305.
[40] Vexler VS, Clément O, Schmitt-Willich H, Brasch RC. Effect of varying the molecular weight of the MR contrast agent Gd-DTPA-polylysine on blood pharmacokinetics and enhancement patterns. J Magn Reson Imaging 1994;4(3):381–8.
[41] Jiang K, Tang H, Mishra PK, Macura SI, Lerman LO. Measurement of murine single-kidney glomerular filtration rate using dynamic contrast-enhanced MRI. Magn Reson Med 2018;79(6):2935–43.
[43] Taxt T, Pavlin T, Reed RK, et al. Using single-channel blind deconvolution to choose the most realistic pharmacokinetic model in dynamic contrast-enhanced MR imaging. Applied Magnetic Resonance 2015;46(6):643–59.
[44] Jiřík R, Bartoš M, Souček K, et al. Dynamic contrast-enhanced MRI using spatial prior knowledge. ISMRM annual meeting 2017. 2017. p. 2895. USA, Honolulu.
[45] Bartoš M, Šorel M, Mangová M, et al. DCE-MRI perfusion analysis with L1-norm spatial regularization. ISMRM-ESMRMB joint annual meeting 2018. France, Paris. 2018. p. 2826.
[46] Sourbron S, Heilmann M, Walczak C, et al. T2*-relaxivity contrast imaging: first results. Magn Reson Med 2013;69(5):1430–7.
[47] Jiřík R, Taxt T, Souček K, et al. Comparison of the ATH and 2CXM models using low- and high-molecular-weight contrast agents in DCE-MRI. Abstracts of ESMRMB Conf., magnetic resonance materials in physics, biology and medicine. vol. 29(Suppl 1). 2016. p. S447–8.